*drones*

*Article*

# Wind Tunnel Balance Measurements of Bioinspired Tails for a Fixed Wing MAV

**Rafael Bardera [1,*], Ángel. A. Rodríguez-Sevillano [2], Estela Barroso [1], Juan Carlos Matías [1] and Suthyvann Sor Mendi [1]**

[1] Instituto Nacional de Técnica Aeroespacial (INTA), 28850 Torrejón de Ardoz, Spain; barrosobe@inta.es (E.B.); matiasgjc@inta.es (J.C.M.); sors@inta.es (S.S.M.)
[2] Escuela Técnica Superior de Ingeniería Aeronáutica y del Espacio, Universidad Politécnica de Madrid, 28040 Madrid, Spain; angel.rodriguez.sevillano@upm.es
* Correspondence: barderar@inta.es

**Abstract:** Bird tails play a significant role in aerodynamics and stability during flight. This paper investigates the use of bioinspired horizontal stabilizers for Micro Air Vehicles (MAVs) with Zimmerman wing-body geometry. Five configurations of bioinspired horizontal stabilizers are presented. Then, 3-component external balance force measurements of each horizontal stabilizer are performed in the wind tunnel. The Squared-Fan-Shaped Horizontal Stabilizer (HSF-tail) is selected as the optimal horizontal stabilizer that provides the highest aerodynamic efficiency during cruise flight while maintaining high longitudinal stability on the vehicle. The integration of the HSF-tail increases the aerodynamic efficiency by more than 6% up to a maximum of 17% compared to the other alternatives while maintaining the lowest aerodynamic drag value during the cruise phase. Furthermore, balance measurements to analyze the influence of the HSF-tail deflection on the aerodynamic coefficients are conducted, resulting in increased lift force and reduced aerodynamic drag with negative tail deflections. Lastly, the experimental data is validated with CFD-RANS steady simulations for low angles of attack, obtaining a relative difference on the measurement around 5% for the aerodynamic drag coefficient and around 10% for the lift coefficient during the cruise flight that demonstrates a high degree of accuracy in the aerodynamic coefficients obtained by external balance in the wind tunnel. This work represents a novel approach through the implementation of a horizontal stabilizer inspired by the structure of the tails of birds that is expected to yield significant advancements in both stability and aerodynamic efficiency, with the potential to revolutionize MAV technology.

**Keywords:** MAV; bioinspired; balance measurements; bird tails; aerodynamics

check for updates

**Citation:** Bardera, R.; Rodríguez-Sevillano, Á.A.; Barroso, E.; Matías, J.C.; Sor Mendi, S. Wind Tunnel Balance Measurements of Bioinspired Tails for a Fixed Wing MAV. *Drones* **2024**, *8*, 16. https://doi.org/10.3390/drones8010016

Academic Editor: Bo Cheng

Received: 8 November 2023
Revised: 14 December 2023
Accepted: 22 December 2023
Published: 10 January 2024



## 1. Introduction

Significant advancements in technology, particularly in both the military and civil fields, have inspired the conception of innovative Micro Air Vehicles (MAV) concepts. They are characterized by their small size and low speed range, similar to birds. The MAV designs are constrained by low Reynolds numbers ($Re = 10^4 - 10^5$), which represents a significant challenge in terms of generating sufficient lift while maintaining control and stability mission requirements [1].

The remarkable similarity between birds and MAVs offers a valuable advantage for adapting bird flight mechanisms to aeronautics. This likeness allows the exploration and application of bird flight principles in these vehicles at a level of detail that is not possible to achieve with larger conventional aircraft [2]. The integration of bird flight mechanisms into MAVs can lead to potential improvements in the maneuverability, versatility, and efficiency of these small-sized vehicles.

Birds exhibit a high ability to modify both the shape of their wings and tail during flight, allowing them to actively control their movements in both lateral and longitudinal directions [3]. The variation in shape and size of bird tails depends on the bird species. Some bird tails are long and pointed, while others are short and rounded. The shape of the bird tail is directly related to flight function. For instance, predatory birds such as hawks or eagles tend to have longer tails for maneuvering and chasing prey, while other birds such as sparrows or woodpeckers have short, rounded tails for greater flight stability [4].

The bird tails are highly specialized aerodynamic structures that play a crucial role in aerodynamics, control, and stability of flight. They act as a rudder, allowing the bird to change its direction in flight and adjust its position in the air. When a bird tilts its tail to one side, it creates a difference in aerodynamic force between the sides, an aerodynamic momentum, which allows turns and changes in direction. The tails generate lift and drag to facilitate the bird's turn in its three axes (yaw, pitch, and roll) while maintaining its stability over an ample range of flight speeds, making them especially useful in low-speed flight. During takeoff and landing maneuvers, the tails provide additional lift that improves wing functions and maintains stability during flight, avoiding control loss [5,6]. However, the increase in aerodynamic drag is related to the size of the tail. Therefore, the larger the tail area, the greater the aerodynamic drag. Tail span will produce an increase in drag, but it does not necessarily contribute significantly to lift [7,8]. As a consequence, to achieve aerodynamically efficient flight, the shape of the tail and its length must be influenced. This breakthrough in the understanding of bird flight, combined with progress in the manufacturing capabilities of such vehicles (including the additive manufacturing of scale models for wind tunnel testing) and their diverse applications, has driven the research and development of vehicles inspired by the biological characteristics of birds [9,10]. Consequently, it becomes necessary to highlight the current state of knowledge surrounding the aerodynamics, flight control, and stability of bio-inspired morphological vehicles. Although there are studies based on MAVs inspired by flapping birds [11,12], the development of bioinspired tail mechanisms in these vehicles is limited. The most advanced vehicle design to incorporate a bio-inspired tail, having progressed through the design, analysis, and flight test phases, is the "LisHawk" vehicle developed by Ajanic [13]. This vehicle was inspired by the Northern Goshawk, a bird known for its agility and maneuverability in forested environments and its stable, high-speed flight in open areas. To replicate these capabilities, the authors designed a model with multiple mechanisms that controlled artificial feathers, enabling adjustments in both wing and tail characteristics. The tail was specifically designed to modify the spreading angle, incidence angle, and rotation around the $Z$-axis (yawing). Experimental tests were conducted using various wing and tail combinations, revealing that a negative tail incidence (upward deflection) resulted in a decrease in lift force. Furthermore, Ajanic discovered that in order to generate sufficient lift to support the body weight and minimize power requirements during steady level flight at slow speeds (below 7.6 m/s), it became essential to increase the spreading and incidence angles while also extending the wings. The results demonstrated that a synergy between these structures facilitated changes in agility, stability, maneuverability, flight speed range, and energy efficiency. The "LisHawk" vehicle enhanced aerodynamic efficiency during flight by dynamically varying the shape of its tail and wing, rendering it versatile and efficient in diverse flight conditions.

Zhen et al. [14] developed a similar tail design to that of the "LisHawk" vehicle, with overlapping elements resembling feathers. This new tail design had a bifurcated shape and the ability to adjust the angle of incidence, spreading angle, and rotation around the longitudinal symmetry axis of the vehicle (rolling) to control the pitch and yaw at the same time. The main advantage of this tail was that it adjusted the stability and maneuverability of the vehicle. Another benefit was the modification of lift and drag characteristics, resulting in an enhancement of the lift-to-drag ratio when the tail area was reduced. It is important to note that, to date, only preliminary simulations have been performed to evaluate its performance.

Recent research, led by Murayama et al. in [15], focused on the development of a tail mechanism inspired by bird tail feathers for bio-inspired vehicles. To evaluate its aerodynamic efficiency, force and moment measurements were conducted using a six-component balance in a wind tunnel, while the attitude of the tail was varied in terms of the pitch, roll, and yaw angles relative to the vehicle. The experimental data confirmed that both the aerodynamic efficiency (in terms of mechanical efficiency) and controllability of the vehicle can be enhanced by modifying the vehicle attitude precisely. In conclusion, their findings suggested that employing tail attitude-based aerodynamic control may be able to cope with the restricting requirements of improving the stability and maneuverability of vehicles. Another important research project in this field was led by Chang [16], who designed an ingenious artificial feather tail mechanism inspired by the rock pigeon (*Columba livia*). This tail design features the ability to adjust the angle of incidence, spreading angle, lateral deviation, and rotation, with the purpose of analyzing how the combination of these adjustable parameters could improve the maneuverability of an unmanned aerial vehicle. A flight test was conducted in which this vehicle was shown to be the first aerial robot to successfully verify its ability to maneuver using lateral tail deviation.

A limited two-degree-of-freedom tail mechanism was proposed by Parga [17] for implementation in a MAV. He developed a V-rotating tail mechanism with control in over rotation around the longitudinal symmetry axis of the vehicle and the angle of incidence. Forces and moments were measured in a wind tunnel, revealing that the rotating tail exhibited a high drag coefficient for a constant angle of attack when the incidence of the tail was increased to 70°, which could effectively function as an air brake.

Other authors investigated the possibility of using MFC (Macro Fiber Composite) actuators on their bioinspired tail designs; thus, Gamble and Inman [18] and Perez-Sanchez et al. [19] used this technology for yaw control over a wide range of slip angles and pitch control.

As can be seen from the literature, the configuration of bird tails presents substantial value in achieving improved longitudinal stability and aerodynamic efficiency during the flight of Micro Air Vehicles (MAVs). This paper investigates the possibility of using bioinspired horizontal stabilizers for MAVs with Zimmerman body-wing geometry.

In particular, the MAV with a Zimmerman wing configuration developed between INTA and ETSIAE (UPM) [20,21] is the object of this study (its main features are detailed in Section 2.1). The main objective is to implement a bioinspired horizontal stabilizer incorporating the benefits of the geometrical characteristics of bird tails through an experimental analysis in the wind tunnel to improve the aerodynamic efficiency and longitudinal stability of the initial MAV. Consequently, five horizontal stabilizers inspired by the main types of bird tails existing in nature are analyzed. These five configurations are the result of a previous numerical parametric study [22], in which the influence of the most relevant tail geometric parameters was analyzed (their characteristics are presented in Section 2.2). In this numerical analysis [23], the Horizontal-Square-Fan-Shaped stabilizer (HSF-tail) provided the highest aerodynamic performance in terms of maximum aerodynamic efficiency during the cruise phase as well as maintaining high longitudinal stability on the vehicle.

In this work, force measurements using a 3-component external balance (designed and manufactured specifically for this MAV vehicle) of each horizontal stabilizer are conducted in an INTA low-speed wind tunnel. The experimental data shows that the Horizontal-Square-Fan-Shaped stabilizer (HSF-tail) provides the highest aerodynamic efficiency during the cruise flight as well as maintaining a high degree of longitudinal stability. This data is validated with the previous numerical data based on CFD-RANS simulations [24], demonstrating high accuracy in the obtained results. Moreover, this paper presents an innovative investigation of emulating avian adaptations in our MAV through the implementation of a horizontal stabilizer inspired by the structure of bird tails. The experimental data represents improvements in the performance of our MAV.

## 2. Bioinspired MAV

### *2.1. Base Model*

The base model of the MAV was designed and developed as a result of a collaboration between INTA (Instituto Nacional de Técnica Aeroespacial) and ETSIAE (Escuela Técnica

Superior d Ingeniería Aeronáutica y del Espacio) at Universidad Politécnica de Madrid (UPM) [22]. The primary aim of this design was to simulate bird flight for enhanced aerodynamic performance in flight (see Figure 1). The initial design of the vehicle had an overall length of $l = 0.30$ m, a wingspan of $b_w = 0.32$ m, and a low-aspect-ratio of $LAR_w = 2.50$ [23,24]. The rest of the geometric characteristics of the base model are presented in Table 1.

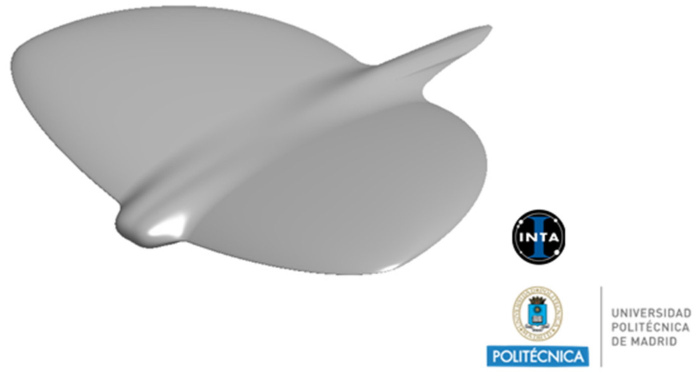


**Figure 1.** Base model developed between INTA and ETSIAE (UPM) [25,26].

**Table 1.** Geometrical features of the base model [24].

| Geometrical Features of the Base Model | Value |
|---|---|
| Fuselage length, $\boldsymbol{l}$ | 0.30 m |
| Fuselage width, $\boldsymbol{d}$ | 0.060 m |
| Dihedral angle, $\boldsymbol{\Gamma_w}$ | 10° |
| Wingspan, $\boldsymbol{b_w}$ | 0.32 m |
| Wing tip chord, $\boldsymbol{c_{t_w}}$ | 0.025 m |
| Wing root chord, $\boldsymbol{c_{r_w}}$ | 0.20 m |
| Wing reference surface, $\boldsymbol{S_{ref}}$ | 0.04 m$^2$ |
| Taper ratio, $\boldsymbol{\lambda}$ | 0.124 |
| Aspect ratio, $\boldsymbol{AR_w}$ | 2.50 |
| Mean aerodynamic chord, ***cma*** | 0.141 m |
| Mean geometrical chord, ***cmg*** | 0.127 m |

The vehicle was designed with a low-aspect-ratio to fly at low Reynolds Numbers ($Re$). To achieve a considerable wing while maintaining the aspect ratio ($AR$) around 2, the Zimmerman configuration emerged as an optimal solution. Moreover, this wing boasts a high theoretical aerodynamic efficiency, $C_L/C_D$, surpassed only by the elliptical planform with the same aspect ratio. The Zimmerman wing is the closest to nature compared with the elliptical planform.

The Zimmerman planform is composed by merging two halves of ellipses at a reference point where one is at $1/4c_{rw}$ and the other is at $3/4c_{rw}$, as illustrated in Figure 2.

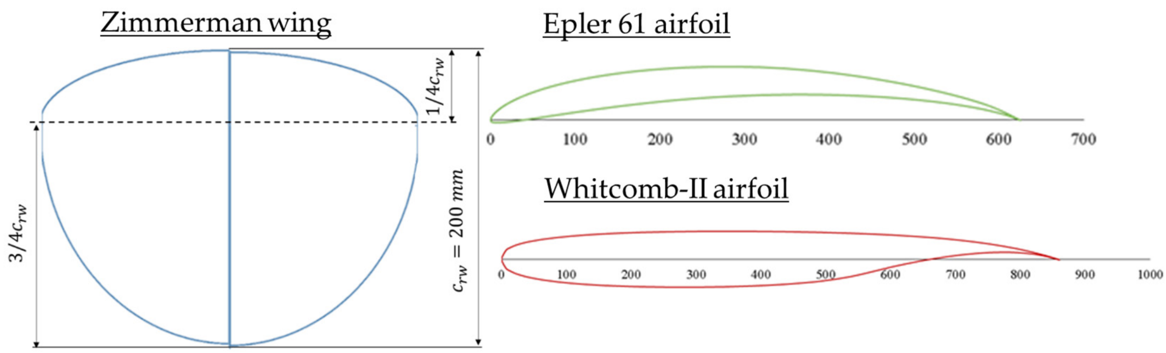


**Figure 2.** Zimmerman wing configuration (**left**) and airfoils (**right**) [23,24].

The wing is composed of Eppler 61 airfoils (Figure 2) due to efficiency behavior in low Reynolds number (Re) flows with progressive stall. Airfoils with small thicknesses compared to their chord have a turbulent boundary layer across most of their operating envelope, causing early boundary layer separation. Despite this leading to certain drawbacks, such as increased aerodynamic drag due to friction, it offers the main advantage of providing the vehicle with a more predictable stall entry. This turbulent regime can delay stall due to the highly energetic nature of the airflow [25,26].

For the fuselage design, Whitcomb II airfoils (Figure 2) were employed. This airfoil enhances the overall lift of the vehicle while maintaining low drag. Additionally, the maximum thickness of this airfoil is 35% of the chord, providing ample cavity to house all mission components such as electronic components, ultra-light cameras, batteries, and electrical engines. The selection of this type of fuselage allows the wing-fuselage joint to maintain the desired continuity, improving the overall aerodynamics of the vehicle.

### *2.2. Bioinspired Horizontal Stabilizers*

The primary objective of this work is to improve the aerodynamic performance ($C_L/C_D$) and longitudinal stability ($C_{m\alpha}$) of the base model. In pursuit of these improvements, the point of inspiration came from bird tails due to their remarkable aerodynamic and flight stability characteristics during flight.

Bird tails exert a substantial influence on aerodynamics and stability, particularly by generating extra lift during slow flight maneuvers such as take-offs and landings. This additional lift accounts for up to 30% of the total lift that sustains birds in the air. Furthermore, bird tails play a significant role in the maneuverability and agility of flight, providing an extra surface that effectively manipulates the air and helps maintain the bird's orientation in three-dimensional flight.

In this paper, five horizontal stabilizer configurations inspired by one or a combination of two bird tails are analyzed experimentally (see Figure 3). The preliminary design of each horizontal stabilizer configuration is detailed in a previous numerical work [22]. The selection of these configurations was conducted by focusing on the main types existing in nature (squared, forked, wedge, pointed, fan, notched, doubled, and rounded).

The Horizontal-Rounded-Fan stabilizer (HRF-tail) is inspired by a combination of rounded and fan-shaped tails; the Horizontal-Squared-Fan stabilizer (HSF-tail) is inspired by square and round shaped-tails; the Horizontal-Forked stabilizer (HFK-tail) is designed based on the forked shaped-tail; the Horizontal-Notched stabilizer (HN-tail) is basically the notched-shaped tail; and finally, the Horizontal-Wedge stabilizer (HW-tail) is similar to the wedge-shaped tail.

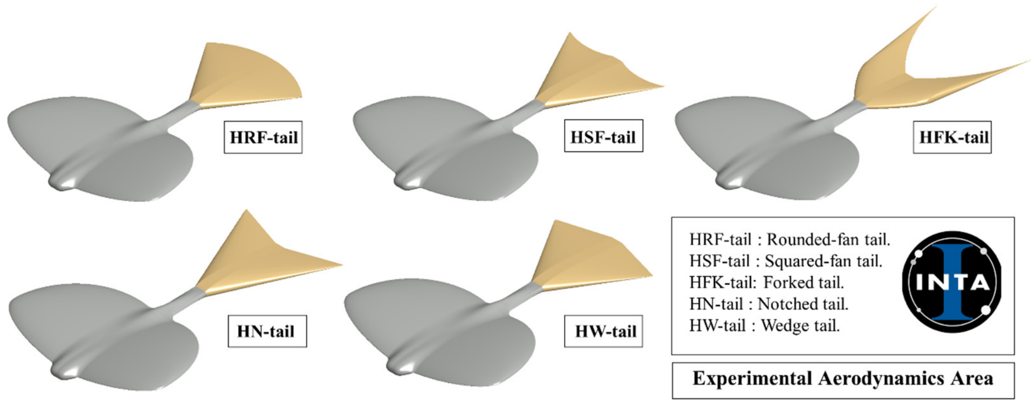


**Figure 3.** Bioinspired Horizontal Stabilizers for the base model [24].

It is important to highlight that all these configurations are designed with a constant horizontal stabilizer surface ($S_h$) and the same airfoil. Therefore, the airfoil selected was the symmetric NACA 0012 airfoil due to its high aerodynamic performance ($C_L$) during cruise flight at low Reynolds numbers. In addition, it is an airfoil used in the design of stabilizers for vehicles of similar dimensions. The design of these horizontal stabilizers, along with the selection of each geometrical parameter, were obtained in a previous numerical work [22].

Table 2 shows the geometric parameters of the bioinspired horizontal stabilizers for the MAV. The variations in span ($b_h$), chord ($c_h$), aspect ratio ($AR_h$), dihedral angle ($\Gamma_h$) and incidence angle ($\delta$) among the horizontal stabilizers came from data obtained in [22]. These values were extracted through a numerical optimization process.

**Table 2.** Geometric parameters of the bioinspired horizontal stabilizers for the MAV [17].

| Configurations | $b_h$ (mm) | $c_{rh}$ (mm) | AR$_h$ | $\Gamma_h$(°) | $\delta$(°) |
|---|---|---|---|---|---|
| HSF-tail | 200 | 170 | 2.10 | 0 | 0 |
| HRF-tail | 196 | 166.6 | 2.10 | −1 | 0 |
| HSF-tail | 200 | 170 | 2.10 | 0 | 0 |
| HFK-tail | 215 | 121 | 2.10 | 3 | 0 |
| HN-tail | 196 | 170 | 2.05 | −1 | 0 |
| HW-tail | 196 | 170 | 2.05 | −1 | 0 |

## 3. Experimental Set-Up

### *3.1. Wind Tunnel*

All experimental tests were conducted in a low-speed wind tunnel, specifically the WK 860060-E model of Westenberg Engineering, located at the Instituto Nacional de Técnica Aeroespacial (INTA). This wind tunnel is an open circuit with a closed circular test section with a diameter of 600 mm and a length of 1200 mm. The airflow speed within the tunnel can be regulated by a frequency variator, reaching a maximum of 60 m/s.

### *3.2. External Balance*

A three-component external balance is used to measure the forces acting on the vehicle in the wind tunnel. This particular external balance was designed, manufactured, and calibrated specifically for this vehicle at INTA.

The external balance consists of a metallic structure that allows decoupling the forces to be measured. This is mainly composed of various mechanisms, including both hollow and solid metal rods, as well as other essential components necessary for the final assembly, such as locking or balancing elements (see Figure 4). The instrumentation is achieved by employing piezoresistive sensors, which consist of three bending load cells fixed to various mechanisms using bearings and bushings. In Figure 4, $LC-1$ is the load cell with a 0–200 g measuring range placed horizontally to measure the pitching moment ($M_y$); $LC-2$ is the load cell that measures the aerodynamic drag force ($D$), it is placed vertically and with a measuring range between 0 and 1000 g; and finally, $LC-3$ is the load cell that measures the lift force ($L$) and is placed horizontally with a 0–200 g measuring range. The forces and pitching moment are obtained along the balance axes ($X, Y, Z$). The lift force ($L$) maintains the direction of the balance axis $Z$, the aerodynamic drag force ($D$) opposes the uniform velocity ($U_\infty$), in the balance axis $X$, and the pitching moment ($M_y$) is obtained at the reference point $O$ along the balance axis $Y$.

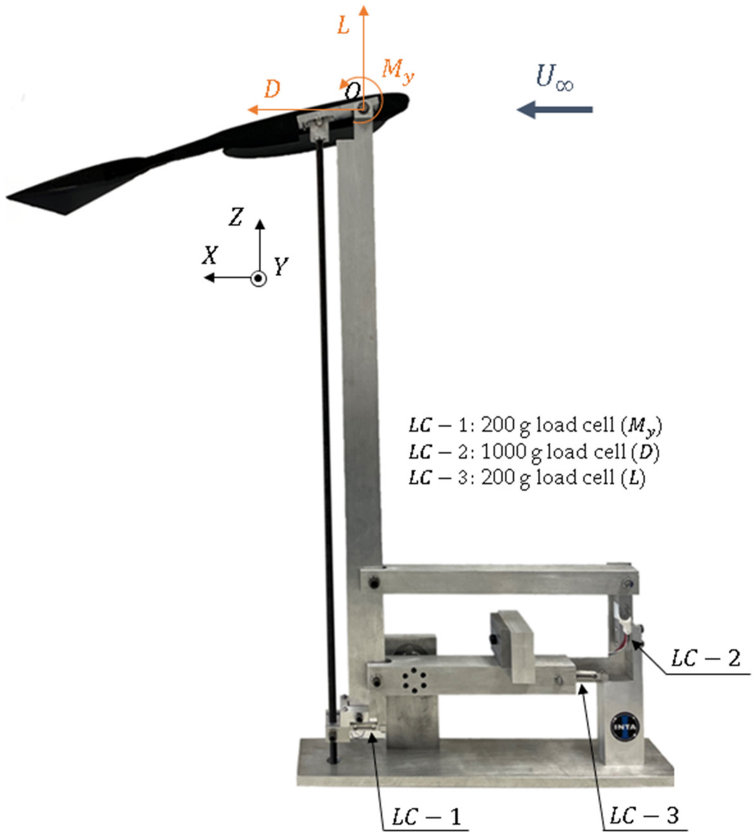


**Figure 4.** Three-component external balance with the semi-MAV model.

The signal from each load cell is processed using HX711 modules, which serve as analog-to-digital converters (A/D converters), in conjunction with an Arduino microcontroller. Each load cell is directly connected to an HX711 module, functioning as an interface between the load cell and the Arduino microcontroller. The HX711 module is responsible for reading the Wheatstone bridge formed by each load cell and converting the analog signal into a digital signal by means of an internal 24-bit A/D converter.

The digital output signals generated by each HX711 module are transmitted to the digital inputs of the Arduino microcontroller. The microcontroller operates on a 5 V power supply sourced from the USB of a computer. Finally, the Arduino microcontroller communicates with the computer so that automated digital data acquisition can be performed.

The data is received in discrete digital units, measured in bits. The calibration process for the external balance enables the correlation between these digital units and the corresponding physical units for each measurement channel.

For each load application case, a record of the three electrical signals is stored for a recording time of 10 s with a sampling rate of 10 Hz, resulting in 100 measurements equally spaced in time. The HX711 A/D converter boasts a resolution of $2^{24} = 16,777,216$, a value significantly higher than the potential error of the load cell. In this case, following the manufacturer's specifications, the load cells are considered to have an error over full-scale equal to $\epsilon = 0.05\% = 0.0005 = 5{\cdot}10^{-4}$, being well below the resolution of the converter. Consequently, the acquisition of the balance signals is verified.

Table 3 shows the standard deviation $s_{F_i}(\%FS)$ of each aerodynamic component according to their respective full scale ($FS$).

**Table 3.** Standard deviation $s_{F_i}(\%FS)$ of each aerodynamic component.

| **Aerodynamic Component $F_i$** | $s_{F_i}(\%FS)$ |
|---|---|
| $L$ | 1.272 |
| $D$ | 1.158 |
| $M_y$ | 0.723 |

### 3.3. Testing Model

To facilitate the performance of wind tunnel tests, the MAV model is manufactured independently of each bioinspired horizontal stabilizer; therefore, the union of both is made with an M3 screw, as seen in Figure 5.

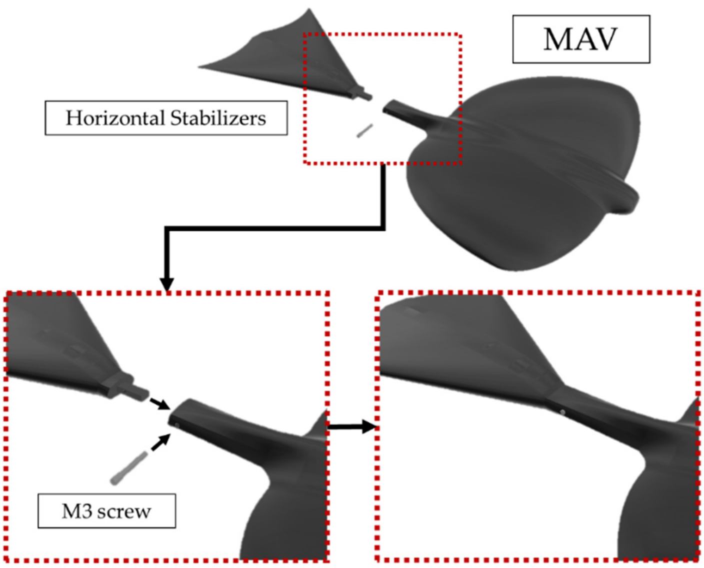


**Figure 5.** MAV and horizontal stabilizer union.

The base model and bioinspired horizontal stabilizers are manufactured using 3D printing technology at INTA. The MAV model is a full-scale model (1:1), as its dimensions fall within 10% of the cross-section of the wind tunnel. PLA (Polylactic Acid) is chosen as the additive material due to its prevalence in such wind tunnel tests and its capability to generate 3D components with exceptional precision and detail.

Since the MAV model and horizontal stabilizers present non-planar shapes, the fabrication process involves dividing each component into two halves along the symmetry axis of the model. This division generates a flat surface, upon which additive material is deposited layer by layer in a vertical direction, that is, from the symmetry axis of the model to the tip of the wing. All material layers are aligned with the free stream of the wind tunnel, thus reducing the surface roughness of the models and preventing premature detachment of the flow stream during wind tunnel testing.

### 3.4. Experimental Tests

After printing both halves of each component, they are assembled using cyano-acrylate glue. As part of the preparation process, a meticulous sanding of the entire surface is performed to minimize surface roughness. Additionally, a thin layer of paint is applied to enhance the uniformity of the surfaces on the models. This finishing process ensures the integrity of the MAV and enhances the accuracy of wind tunnel testing results. Figure 6 shows the bioinspired horizontal stabilizers manufactured by 3D printing for wind tunnel testing.

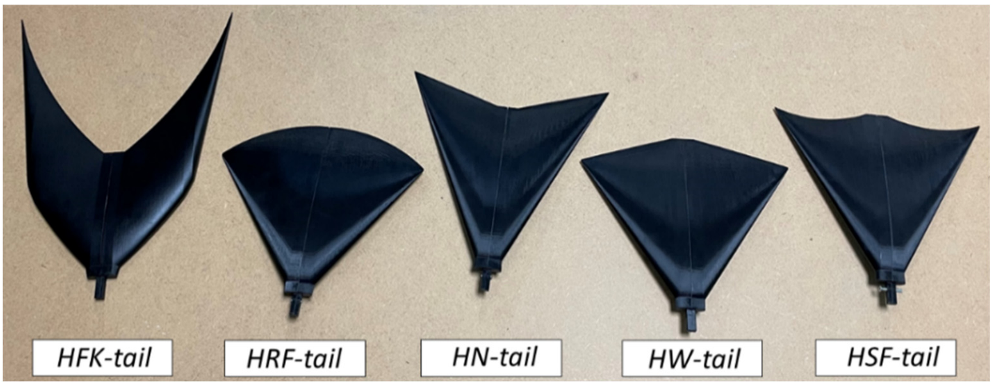


**Figure 6.** Bioinspired horizontal stabilizers for wind tunnel testing.

Figure 7 shows the assembly of the vehicle and the external balance in the wind tunnel for the cruise condition ($\alpha = 0°$). The vertical rod, connected to the model, was supported by a streamlined support strut to minimize flow perturbations during the wind tunnel testing. This streamlined support strut was composed of symmetry airfoils (NACA 0012) and made of PLA using 3D printing.

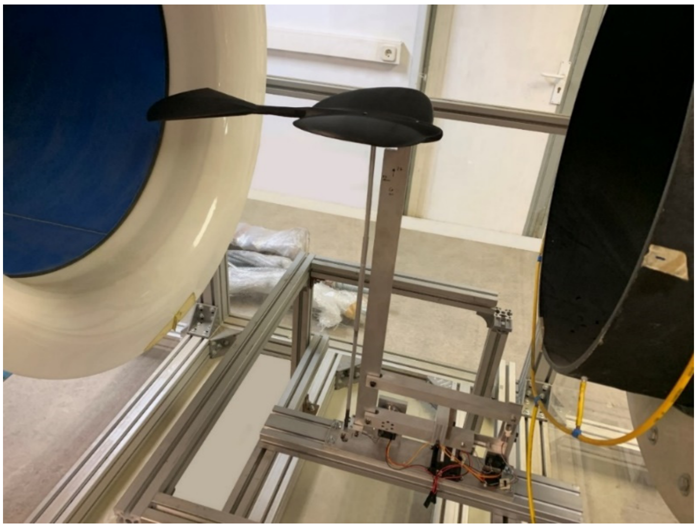

**Figure 7.** MAV attached to the external balance inside the wind tunnel at INTA.

The length of the vertical rod was chosen to place the external balance outside the test section of the wind tunnel while maintaining the MAV model in the center of it to be aligned with the wind tunnel axis. Moreover, a wooden board was required to place the streamlined support strut, thus avoiding any contact with the external balance.

The experimental tests consisted of obtaining the lift and aerodynamic drag forces and the pitching moment around the vehicle with the five bioinspired horizontal stabilizers. These tests were conducted with a free stream velocity of $U_\infty = 10$ m/s, which corresponds to a Reynolds number ($Re$) based on the maximum wing chord ($c_{rw} = 0.2$ m) of $Re = \frac{\rho_\infty \cdot U_\infty . c_{rw}}{\mu_\infty} = 1.37 \cdot 10^5$ (where $\rho_\infty$ is the air density and $\mu_\infty$ the air dynamic viscosity). Measurements were taken in the range of angles of attack, spanning from $\alpha = -5°$ to $\alpha = 30°$ with an interval of 5°.

## 4. Analysis of the Results

In this section, a brief overview of the coefficients assessed through balance-force measurements in the wind tunnel is presented.

The lift coefficient ($C_L$) measures the capacity of the vehicle to generate enough lift force for sustained flight; therefore, $C_L$ should have high values (Equation (1)).

The aerodynamic drag coefficient ($C_D$) quantifies the resistance faced by the vehicle when moving through the air (Equation (2)). A low value of this coefficient indicates that the vehicle is more energy-efficient, as it reduces the aerodynamic drag.

The pitching moment coefficient ($C_m$) takes into account the stability of the vehicle; that is, it indicates the tendency of the vehicle to pitch during flight (Equation (3)).

Knowledge of these three coefficients is essential for the effective design and control of the bioinspired MAV, ensuring its ability to fly safely and efficiently. As a result, this paper focuses on the analysis of the following three coefficients obtained experimentally.

$$C_L = \frac{L}{\frac{1}{2}\rho_\infty U_\infty^2 S_{ref}} \tag{1}$$

$$C_D = \frac{D}{\frac{1}{2}\rho_\infty U_\infty^2 S_{ref}} \tag{2}$$

$$C_m = \frac{M}{\frac{1}{2}\rho_\infty U_\infty^2 S_{ref}\bar{c}} \tag{3}$$

where $L$ is the lift force, $D$ the aerodynamic drag, $M$ the pitching moment, $\rho_\infty$ the air density, $S_{ref}$ the wing reference surface, $\bar{c}$ the mean aerodynamic chord, and $U_\infty$ the free stream velocity.

Figure 8 shows the forces acting on the MAV vehicle with the MAV axes ($X_b$, $Y_b$, $Z_b$) and balance axes ($X$, $Y$, $Z$).

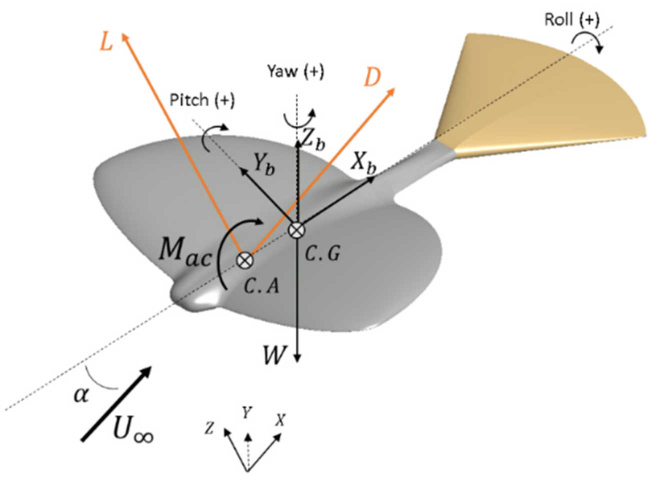


**Figure 8.** Forces acting on the MAV with the Horizontal Rounded-Fan stabilizer (HRF-tail).

### *4.1. Measurements with External Balance*

Figure 9 shows the lift coefficient ($C_L$) obtained with the five bioinspired horizontal stabilizers by force balance measurements in the wind tunnel, with zero tail incidence angle.

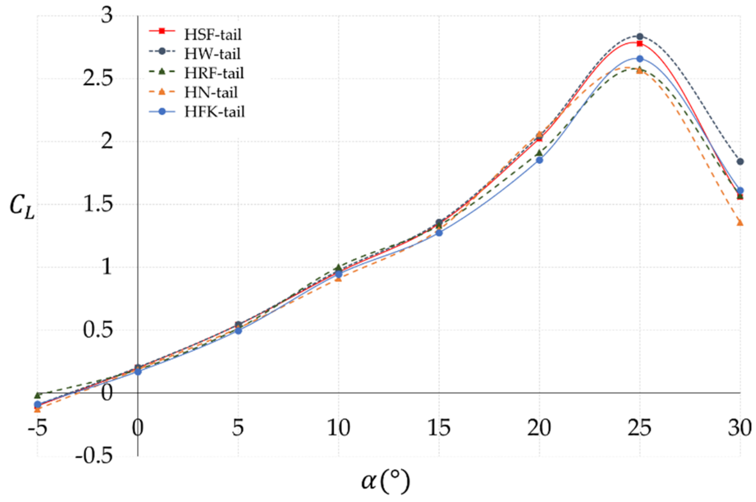


**Figure 9.** Lift coefficient ($C_L$) for the five bioinspired horizontal stabilizers measured by force balance in the wind tunnel at INTA ($\delta = 0°$).

It is clearly observed that the lift coefficient ($C_L$) increases with the angle of attack until reaching a maximum value ($C_{Lmax}$) when $\alpha = 25°$. This increase in lift coefficient is practically linear up to low angles of attack ($\alpha \leq 20°$). After the maximum lift coefficient ($C_{Lmax}$), there is a sharp decrease in lift, which corresponds to the stall condition, that is, the lift is reduced rapidly, therefore the vehicle is not able to fly.

At low angles of attack ($\alpha \leq 10°$), the lift coefficient shows similar values between all horizontal stabilizers. However, when the angle of attack is higher ($\alpha > 10°$), a slight difference between them can be appreciated. The maximum value of $C_{Lmax} = 2.834$ is obtained for the Horizontal-Wedge-Shaped stabilizer (HW-tail), being 1.90% higher than the Square-Fan-Shaped stabilizer (HSF-tail), being 6.20% higher than the Forked-Shaped stabilizer (HFK-tail), 9.19% higher than the Rounded-Fan-Shaped stabilizer (HRF-tail), and 9.48% higher than the Notched-Shaped stabilizer (HN-tail).

Figure 10 shows the aerodynamic drag coefficient ($C_D$) obtained with the five bioinspired horizontal stabilizers by force balance measurements in the wind tunnel.

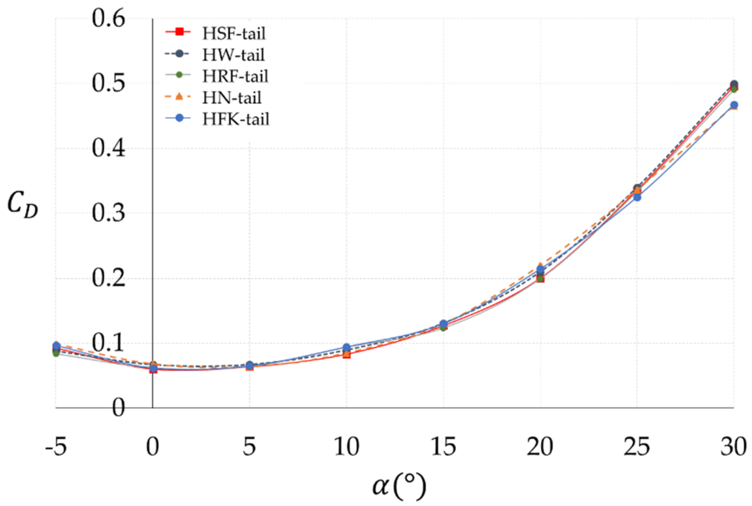


**Figure 10.** Aerodynamic drag coefficient ($C_D$) for the five bioinspired horizontal stabilizers measured by force balance in the wind tunnel at INTA ($\delta = 0°$).

In all bioinspired horizontal stabilizers, the values of the aerodynamic drag coefficient ($C_D$) at all angles of attack are practically the same; only HFK and HN-tails show slight differences at very high angles of attack, around $\alpha = 30°$.

The aerodynamic drag coefficient ($C_D$) increases with the angle of attack. At low angles of attack, between $-5° \leq \alpha \leq +5°$, the aerodynamic drag coefficient presents a typical value of these vehicles, with values less than 0.1. The minimum drag coefficient ($C_{Dmin}$) is obtained during the cruise phase between $0° \leq \alpha \leq +5°$.

Figure 11 shows the polar curve obtained for the five bioinspired horizontal stabilizers by force balance measurements in the wind tunnel.

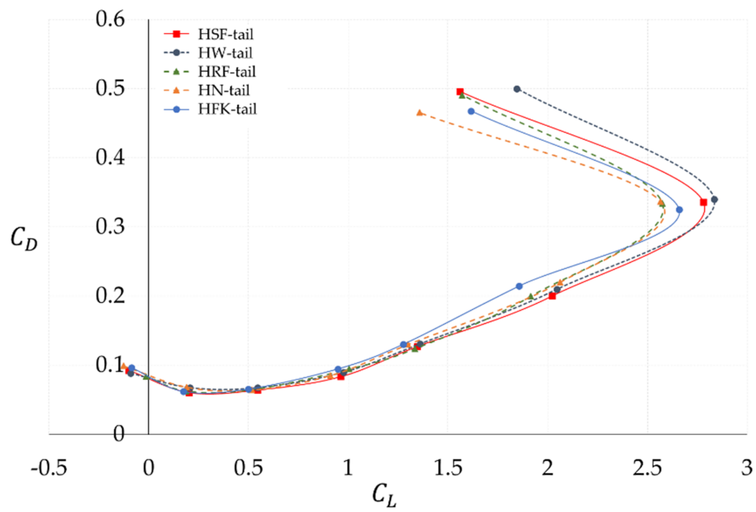


**Figure 11.** Polar curve ($C_D - C_L$) for the five bioinspired horizontal stabilizers measured by force balance in the wind tunnel at INTA ($\delta = 0°$).

Figure 12 shows the aerodynamic efficiency ($C_L/C_D$) obtained for the five bioinspired horizontal stabilizers by force balance measurements in the wind tunnel.

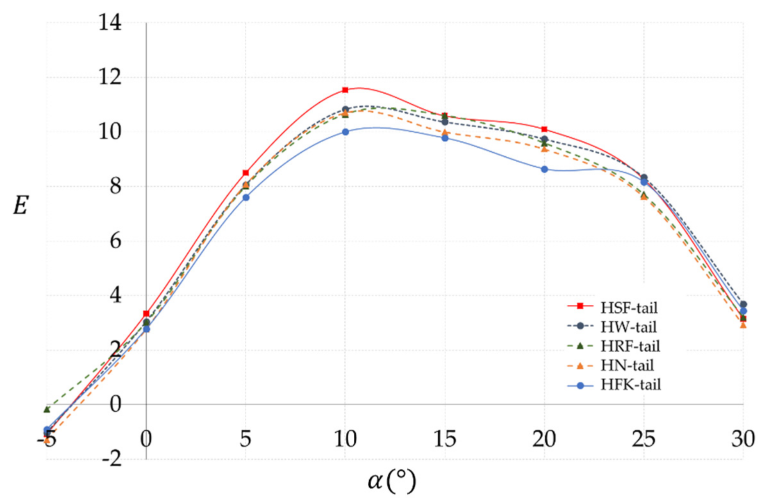


**Figure 12.** Aerodynamic efficiency ($E$) for the five bioinspired horizontal stabilizers measured by force balance in the wind tunnel at INTA ($\delta = 0°$).

The aerodynamic efficiency values vary slightly among the different horizontal stabilizers across all angles of attack. However, all of them present a similar trend, that is, as the angle of attack increases, the efficiency also increases until reaching a maximum value ($E_{max}$) at the angle of attack of $\alpha = 10°$. In this flight condition, preferable for take-off and landing flight phases, the highest value of $E_{max}$ is achieved with the HSF-tail ($E_{max} = 11.53$) followed in descending order by the configurations of HW, HN, HRF, and HFK.

For higher angles of attack ($\alpha > 10°$), the aerodynamic efficiency decreases progressively until reaching the stall condition, where a sharp loss of efficiency occurs.

The most interesting region is presented for the cruise flight ($0° \leq \alpha \leq +5°$), where again the highest value of aerodynamic efficiency is obtained with the Squared-Fan-Shaped stabilizer (HSF-tail). As a consequence, this horizontal stabilizer becomes the best candidate for implementation on the vehicle, as it has the potential to enhance the autonomy and range of the vehicle.

Figure 13 shows the pitching moment coefficient ($C_m$) obtained for the five bioinspired horizontal stabilizers by force balance measurements in the wind tunnel. These measurements are taken at the reference point $O$, located at $x_O = 0.050\ m$ from the nose of the MAV (Figure 14). This is a fixed point joining the MAV and the external balance and is located near the aerodynamic center of the vehicle ($x_{ac}$).

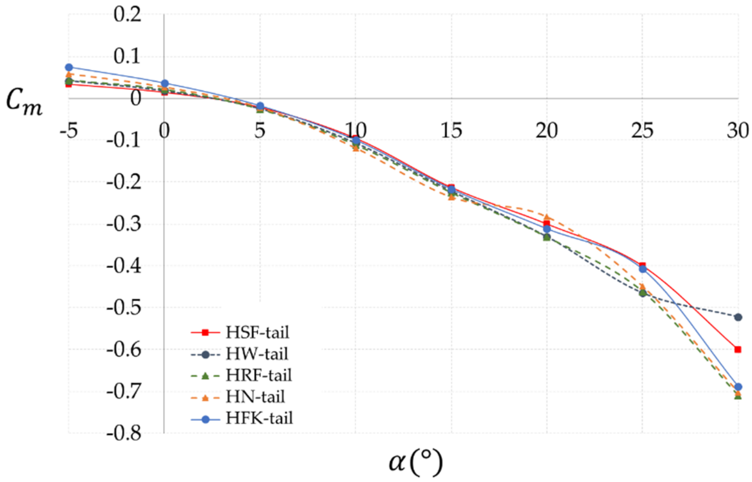


**Figure 13.** Pitching moment coefficient ($C_m$) for the five bioinspired horizontal stabilizers measured by force balance in the wind tunnel at INTA ($\delta = 0°$).

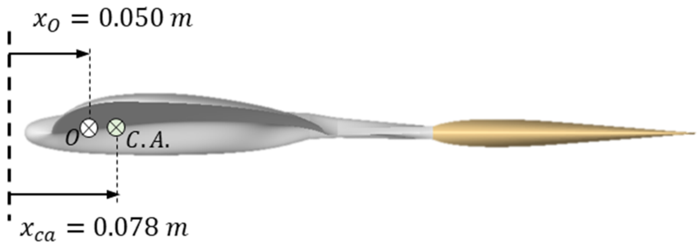


**Figure 14.** Position of the reference point $O$ where the pitching moment is measured.

The aerodynamic center of the vehicle ($x_{ac}$) can be easily calculated by applying the following expression:

$$\frac{x_{ac}}{cma} = \frac{x_O}{cma} - \frac{\left(\frac{\partial C_{mO}}{\partial \alpha}\right)}{\left(\frac{\partial C_L}{\partial \alpha}\right)} \quad (4)$$

where $\left(\frac{\partial C_{mO}}{\partial \alpha}\right)$ is the slope of the pitching moment coefficient obtained directly from Figure 14 $\left(\frac{\partial C_{mO}}{\partial \alpha} = -0.02\right)$ and $\left(\frac{\partial C_L}{\partial \alpha}\right)$ is the slope of the lift coefficient obtained from Figure 9 $\left(\frac{\partial C_L}{\partial \alpha} = 0.1\right)$. Therefore, the aerodynamic center of the vehicle is placed at $x_{ac} = 0.078$ from the nose of the vehicle (see Figure 13).

The five bioinspired stabilizers show similar values of $C_m$ during all angles of attack. Notably, these configurations are longitudinal stables, as the curves intersect with the $X$-axis with negative slopes ($C_{m\alpha}$) during the cruise flight phase. Consequently, the MAV can maintain stable and level flight with relatively low angles of attack ($0° \leq \alpha \leq 5°$) without requiring a constant force on the horizontal stabilizer to maintain its attitude during flight. In other words, the MAV naturally maintains equilibrium during the cruise flight, avoiding a tendency to ascend or descend. This natural equilibrium, with $C_m = 0$ during the cruise flight, is crucial for both the efficiency and safety of the vehicle.

It can be seen that all bioinspired horizontal stabilizers present $C_m = 0$ with an angle of attack between $2° \leq \alpha \leq 4°$.

A summary of the relevant aerodynamic parameters with the values of the best horizontal stabilizers is presented in Table 4.

**Table 4.** Aerodynamic parameters of the best horizontal stabilizers.

| Aerodynamic Parameters | Value | Horizontal Stabilizer |
|---|---|---|
| $C_{Lmax}$ | 2.83 | HN-tail |
| $C_{L0}$ | 0.20 | HW-tail |
| $C_{Dmin}$ | 0.06 | HSF-tail |
| $E_{max}$ | 11.53 | HSF-tail |
| $E_0$ | 3.33 | HSF-tail |

Table 5 presents the variations of these aerodynamic parameters between different horizontal stabilizers, providing a clearer representation of how these parameters increase or decrease. Based on this data, it can be concluded that the Squared-Fan-Shaped stabilizer (HSF-tail) is the selected implementation solution for the MAV.

**Table 5.** Aerodynamic parameter variation.

| Variation | HN-Tail | HW-Tail | HSF-Tail | HRF-Tail | HFK-Tail |
|---|---|---|---|---|---|
| $\Delta C_{Lmax}$ | ↓ 9.48% | - | ↓ 1.90% | ↓ 9.19% | ↓ 6.20% |
| $\Delta C_{L0}$ | ↓ 8.42% | - | ↓ 2.18% | ↓ 8.68% | ↓ 16.16% |
| $\Delta C_{Dmin}$ | ↑ 12.98% | ↑ 12.01% | - | ↑ 3.28% | ↑ 2.74% |
| $\Delta E_{max}$ | ↓ 7.20% | ↓ 6.06% | - | ↓ 7.67% | ↓ 13.27% |
| $\Delta E_0$ | ↓ 17.13% | ↓ 8.73% | - | ↓ 9.61% | ↓ 16.57% |

Table 6 summarizes the values of the aerodynamic efficiency ($E_0$) during cruise flight ($\alpha = 0°$) for the five bioinspired horizontal stabilizers.

**Table 6.** Aerodynamic efficiency in cruise flights.

| Efficiency | HW-Tail | HN-Tail | HSF-Tail | HRF-Tail | HFK-Tail |
|---|---|---|---|---|---|
| $E_0$ | 3.04 | 2.76 | 3.33 | 3.01 | 2.78 |
| | 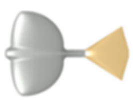 | 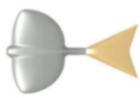 | 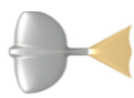 | 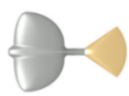 | 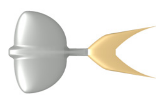 |

### 4.2. Deflection-Horizontal Stabilizer

After selecting the horizontal stabilizer HSF-tail as the solution for implementation on the MAV, a detailed study of stabilizer deflection is conducted to investigate the influence of aerodynamic forces under various conditions. This experimental analysis is crucial for acquiring deep aerodynamic insights and ensuring the longitudinal stability and control of the vehicle during flight.

The horizontal stabilizer is tested at different angles of incidence, from $\delta = -10°$, to $\delta = +10°$, with an interval of 5°. When the angle of incidence is negative, the stabilizer exhibits an upward deflection, whereas when it deflects downward, the angle of incidence is positive (see Figure 15). Within each angle of incidence, the entire range of angles of attack is studied.


**Figure 15.** Sign criteria for the tail angle of incidence ($\delta$).

Figure 16 shows the lift coefficient ($C_L$) for the HSF-tail with all angles of incidence. It is obvious that as the angle of incidence becomes negative (upward deflection), the lift coefficient decreases in all ranges of angles of attack compared to the stabilizer with a zero angle of incidence (orange curve). On the contrary, when the angle of incidence is positive (downward deflection), the lift coefficient is higher than that of the zero angle of incidence. The data clearly shows that the greater lift coefficient is obtained at an angle of incidence of $\delta = +10°$.

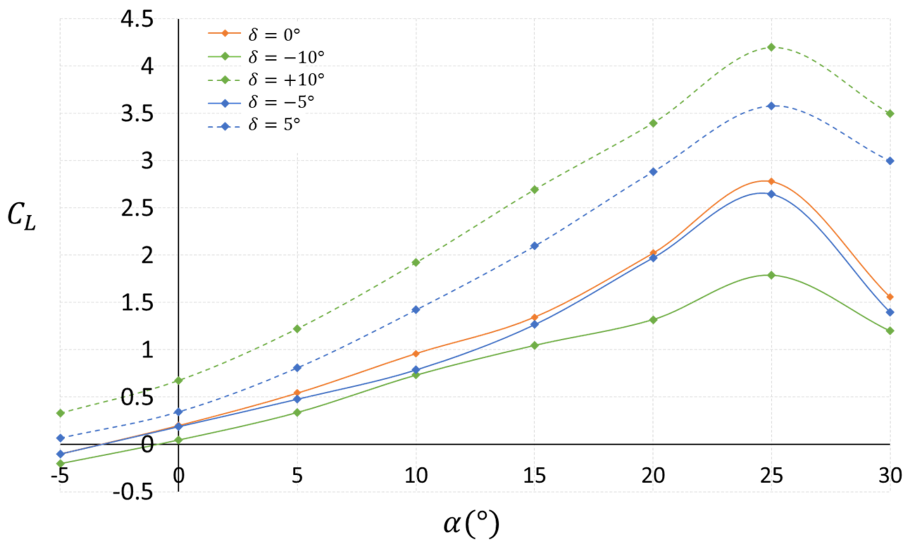


**Figure 16.** Lift coefficient ($C_L$) of the Horizontal-Squared-Fan-Shaped stabilizer (HSF−tail) for various angles of incidence measured by force balance measurements in the wind tunnel at INTA.

Similar to the impact on lift force, the variation of the horizontal stabilizer deflection will also influence the aerodynamic drag characteristics. Figure 17 shows the aerodynamic drag coefficient ($C_D$) for the HSF-tail at various angles of incidence.

The aerodynamic drag variation due to horizontal stabilizer deflection will depend on the angle of attack, the orientation of the wing, and the flight conditions. In this context, it is observed how negative angles of incidence (upward deflection) result in an increased aerodynamic drag coefficient when compared to the zero angle of incidence ($\delta = 0°$). In contrast, positive angles of incidence yield reduced values of aerodynamic drag over the entire range of angles of attack in comparison to the zero angle of incidence. The lowest aerodynamic drag coefficient is achieved when employing an angle of incidence of $\delta = +10°$.

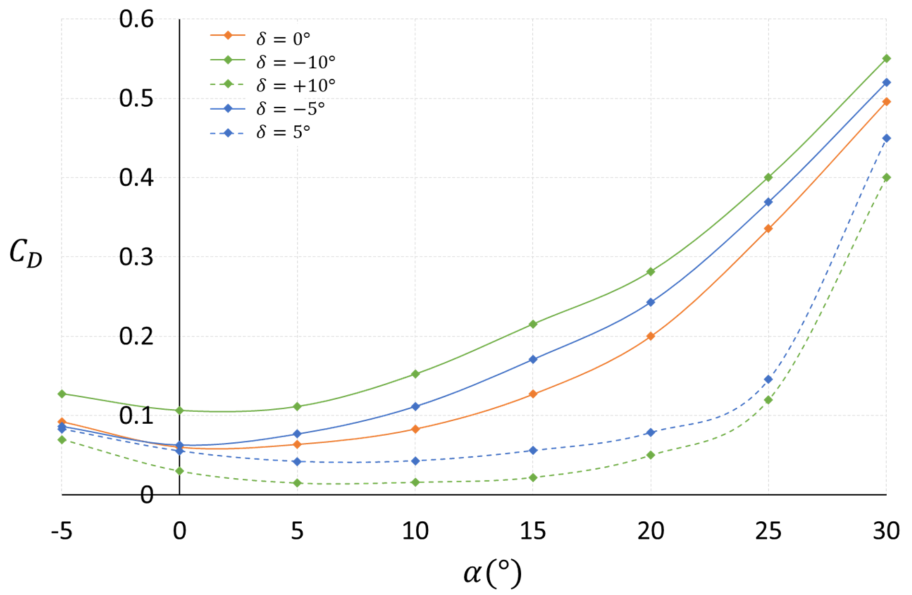


**Figure 17.** Aerodynamic drag coefficient ($C_D$) of the Horizontal-Squared-Fan-Shaped stabilizer (HSF−tail) for various angles of incidence obtained by force balance measurements in the wind tunnel at INTA.

Figure 18 shows the pitching moment coefficient $C_m$ curve for all angles of incidence measured at the reference point $O$. As in the previous cases, adjusting the horizontal stabilizer deflection leads to observable changes in the pitching moment coefficient. Deflection of the stabilizer should shift the pitching moment curve by adjusting the trim angle of attack (the angle of attack at which the pitching moment coefficient is zero) without substantially changing the pitching moment slope.

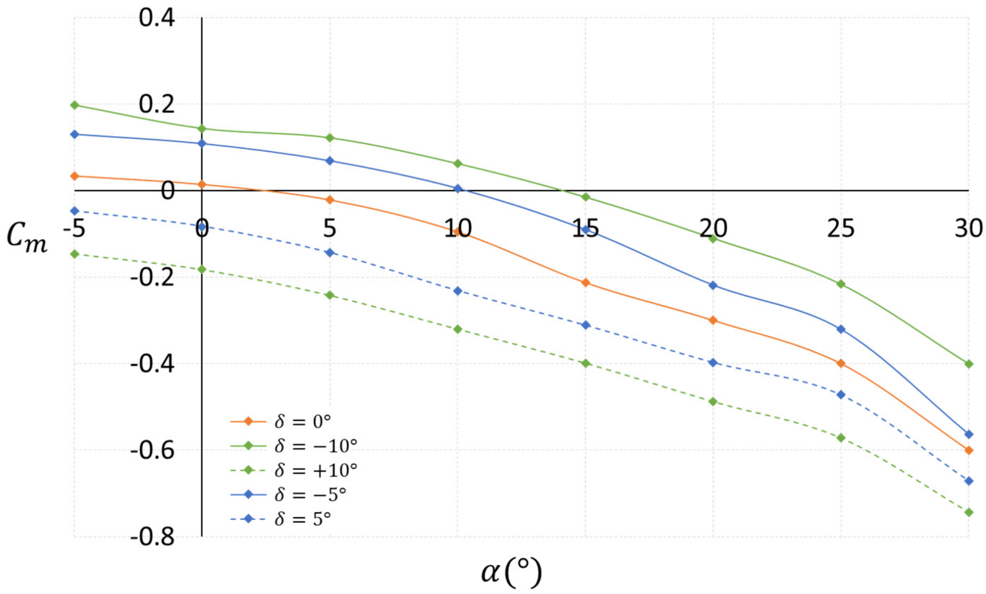


**Figure 18.** Pitching moment coefficient ($C_m$) of the Horizontal-Squared-Fan-Shaped stabilizer (HSF−tail) for various angles of incidence obtained by force balance measurements in the wind tunnel at INTA.

In the case of zero angle of incidence ($\delta = 0°$), the moment coefficient curve intercepts the $X$-axis at approximately at $\alpha = 3°$, providing a MAV longitudinal stable under this condition. As the angle of incidence becomes negative, the curves shift upward with respect to the curve corresponding to the zero angle of incidence, increasing the pitching moment coefficient. The opposite occurs when the angle of incidence becomes positive, the curves shift downward, and the value of $C_m$ decreases.

### *4.3. Experimental Validation*

A validation of the experimental data is required. The balance measurements are compared with CFD data obtained in a previous study [24]. This comparative analysis is conducted with the Horizontal-Squared-Fan-Shaped stabilizer (HSF-tail).

Figure 19 shows the lift coefficient curves ($C_L$) for all angles of attack, except for those near the stall condition ($\alpha \sim 25°$). It is clearly observed that the values of lift coefficient obtained by both methods are fairly similar up to $\alpha < 20°$. The numerical values are slightly higher than those obtained with the external balance in the wind tunnel. It could be that the CFD numerical calculation is overestimating this coefficient due to the turbulence model selected (k-$\omega$ SST) or the lack of resolution in the 3D computational mesh. The maximum relative difference of 23.77% is obtained at $\alpha = 5°$, while the minimum relative difference of 3.95% is obtained at α = 15°. It can be verified that there is high accuracy in the measurement of the lift coefficient when the angles of attack are less than $\alpha < 20°$.

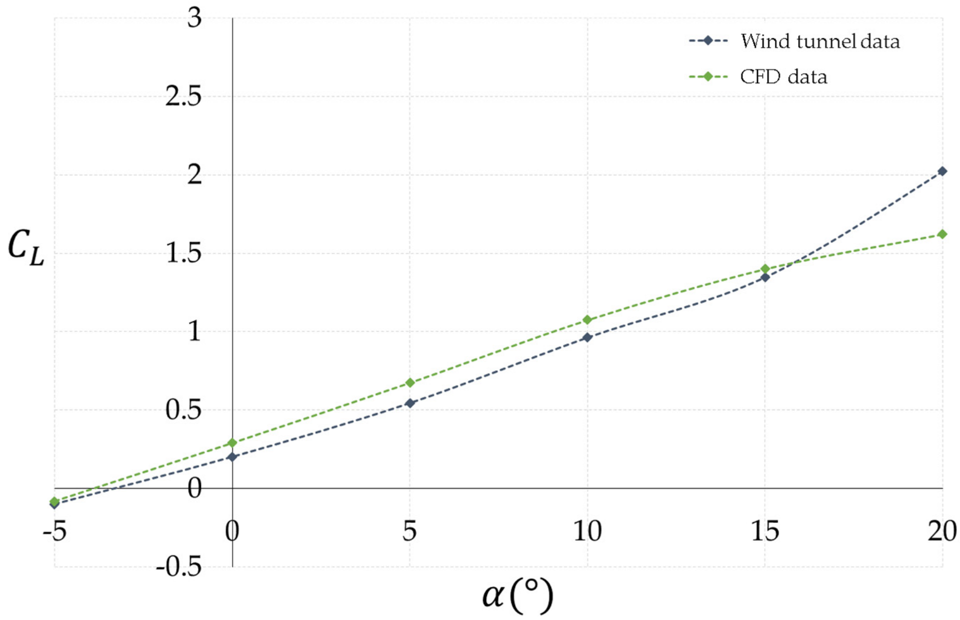


**Figure 19.** Lift coefficient curves obtained with external wind tunnel balance and CFD simulations of the Horizontal-Squared-Fan-Shaped stabilizer (HSF−tail).

Figure 20 shows the aerodynamic drag coefficient curves ($C_D$) for low angles of attack ($-5° \leq \alpha \leq +5°$), as this research is mainly focused on the cruise condition. In this range of angles of attack, the relative difference of 5.20% is obtained when the angle of attack is $\alpha = 0°$, and the minimum relative difference is 1.20% when $\alpha = -5°$.

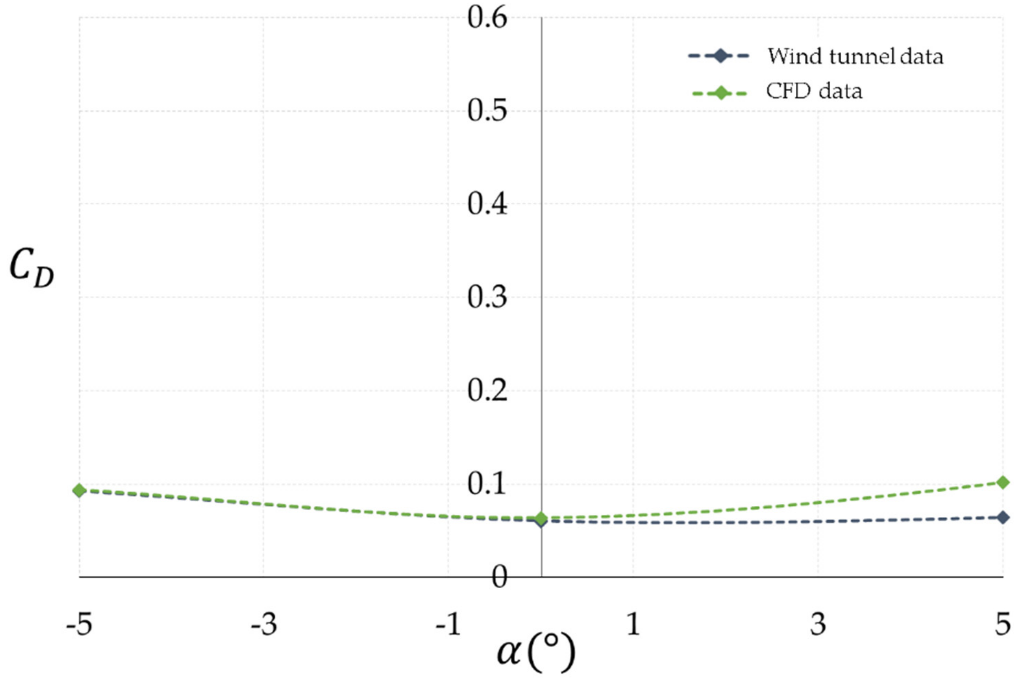


**Figure 20.** Aerodynamic drag coefficient curves obtained with external wind tunnel balance and CFD simulations of the Horizontal-Squared-Fan-Shaped stabilizer (HSF−tail).

## 5. Conclusions

Inspiration from nature to develop MAVs is a promising trend in the field of aviation. This novel concept, known as bio-inspiration, tends to search for efficient and adaptive solutions that evolution has perfected over millions of years. This work presents an experimental analysis of horizontal stabilizers inspired by the most typical tails of birds (rounded, fan, notched, forked, squared, and wedge-shaped tails) due to their relevance and effectiveness in natural aviation. As a consequence, five designs of horizontal stabilizers inspired by one or a combination of two bird tails are analyzed in this paper.

The primary aim is to integrate a horizontal stabilizer, beneficiating from bird tail properties, to enhance longitudinal stability and aerodynamic efficiency during the cruise phase of a Micro Air Vehicle (MAV) featuring a Zimmerman body-wing design, developed between INTA (Instituto Nacional de Técnica Aeroespacial) and ETSIAE (Escuela Técnica Superior de Ingeniería Aeronáutica y del Espacio). Force measurements are conducted utilizing a 3-component external balance installed in a wind tunnel at INTA. This balance, composed of three load cells, allows for the measurement of the lift, aerodynamic drag, and pitching moment across a range of angles of attack. Experimental data indicates that the Horizontal-Squared-Fan-Shaped stabilizer (HSF-tail) attains the maximum aerodynamic efficiency during cruise flight. Consequently, the HSF-tail is selected as the optimal solution for integration into the MAV vehicle. Its implementation is expected to extend the operational range and autonomy of the MAV while ensuring high longitudinal stability during cruise flights. Moreover, force measurements are conducted using the HSF-tail at different angles of incidence to assess how horizontal stabilizer deflection impacts the aerodynamic forces. The data indicate that negative stabilizer deflections result in elevated lift coefficient ($C_L$) values, concurrently reducing the aerodynamic drag coefficient ($C_D$).

Finally, experimental data validation is conducted with CFD-RANS steady simulations (obtained in a previous study). During the cruise flight, the relative difference obtained for $C_D$ is around 5%, while for $C_L$ it is around 10%. It can be concluded that there is a high degree of accuracy in the measurements of the aerodynamic coefficients obtained by the external balance in the wind tunnel. It is important to clarify that there is a limitation in the experimental results since this data is obtained for a specific geometry model (Zimmerman wing-body geometry) with predefined boundary conditions and assumptions. Consequently, it would be highly desirable to test the HSF-tail configuration on similar-sized vehicles with different wing configurations.

The paper conclusively establishes the feasibility of integrating a horizontal stabilizer design, influenced by the geometrical advantages observed in avian tails (specifically, a synergy of Rounded-Fan tails). This integration notably enhances the aerodynamic efficiency and longitudinal stability of a Micro Air Vehicle with a Zimmerman wing-body configuration.

**Author Contributions:** Conceptualization, R.B., Á.A.R.-S. and S.S.M.; methodology, R.B., Á.A.R.-S. and S.S.M.; software, J.C.M. and E.B.; validation, R.B., Á.A.R.-S., J.C.M., E.B. and S.S.M.; formal analysis, R.B., Á.A.R.-S., J.C.M. and E.B.; investigation, R.B., Á.A.R.-S., J.C.M., E.B. and S.S.M.; resources, J.C.M. and E.B.; data curation, R.B., Á.A.R.-S., J.C.M., E.B. and S.S.M.; writing—original draft preparation, R.B., Á.A.R.-S., J.C.M., E.B. and S.S.M.; writing—review and editing, R.B., Á.A.R.-S., J.C.M., E.B. and S.S.M.; visualization, R.B.; supervision, R.B.; project administration, R.B.; funding acquisition, R.B. All authors have read and agreed to the published version of the manuscript.

**Funding:** This research received no external funding.

**Data Availability Statement:** Data are contained within the article.

**Acknowledgments:** We thank all engineers and analysts of the Aerodynamics Department of ‘‘Instituto Nacional de Técnica Aeroespacial Esteban Terradas” (INTA) and Escuela Técnica Superior de Ingeniería Aeronáutica y del Espacio (ETSIAE).

**Conflicts of Interest:** The authors declare no conflict of interest. The funders had no role in the design of the study; in the collection, analyses, or interpretation of data; in the writing of the manuscript, or in the decision to publish the results.

## References

1. Hassanalian, M.; Abdelkefi, A. Classifications, applications and design challenges of drones: A review. *Prog. Aerosp. Sci.* **2017**, *91*, 99–131. [CrossRef]
2. Harvey, C.; Inman, D.J. Aerodynamic efficiency of gliding birds vs. comparable UAVs: A review. *Bioinspiration Biomim.* **2021**, *16*, 031001. [CrossRef] [PubMed]
3. Xu, X.; Zhou, Z.; Dudley, R.; MacKem, S.; Chuong, C.M.; Erickon, G.M.; Varricchio, D.J. An integrative approach to understanding bird origins. *Science* **2014**, *346*, 1253293. [CrossRef] [PubMed]
4. Balmford, A.; Jones, I.L.; Thomas, A.L.R. On avian asymmetry: Evidence of natural selection for symmetrical tails and wings in birds. *Proc. Biol. Sci.* **1993**, *252*, 245–251. [CrossRef]
5. Sachs, G. Tail effect on yaw stability in birds. *J. Theor. Biol.* **2007**, *249*, 464–472. [CrossRef] [PubMed]
6. Thomas, A.R.L. On the aerodynamics of birds' tails. *Pilos. Trans. Biol. Sci.* **1993**, *340*, 361–380. [CrossRef]
7. Ltshuler, D.L.; Bahlman, J.W.; Dakin, R.; Gaede, A.H.; Goller, B.; Lentink, D.; Segre, P.S.; Skandalis, D.A. The biophysics of bird flight: Functional relationships integrate aerodynamics, morphology, kinematics, muscles, and sensors. *Can. J. Zool.* **2015**, *93*, 961–975. [CrossRef]
8. Thomas, A.L.R. The flight of birds that have wings and a tail: Variable geometry expands the envelope of flight performance. *J. Theor. Biol.* **1996**, *183*, 237–245. [CrossRef]
9. Ward, T.A.; Fearday, C.J.; Salami, E.; Binti Soin, N. A bibliometric review of progress in micro air vehicle research. *Int. J. Micro Air Veh.* **2017**, *9*, 146–165. [CrossRef]
10. Ariyanto, M.; Setiawan, J.D.; Prabowo, T.; Haryanto, I. Design of a Low-Cost Fixed Wing UAV. In Proceedings of the 2nd International Joint Conference on Advanced Engineering and Technology (IJCAET 2017) and International Symposium on Advanced Mechanical and Power Engineering (ISAMPE 2017), Bali, Indonesia, 24–26 August 2017.
11. Keennon, M.; Klingebiel, K.; Won, H. Development of the nano hummingbird: A tailless flapping wing micro air vehicle. In Proceedings of the 50th AIAA Aerospace Sciences Meeting Including the New Horizons Forum and Aerospace Exposition, Nashville, TN, USA, 9–12 January 2012; p. 588.
12. Folkertsma, G.A.; Straatman, W. Robird A Robotic Bird of Prey. *IEEE Robot. Autom. Mag.* **2017**, *24*, 22–29. [CrossRef]
13. Ajanic, E.; Feroskhan, M.; Mintchev, S.; Noca, F.; Floreano, D. Bioinspired wing and tail morphing extends drone flight capabilities. *Sci. Robot.* **2020**, *5*, eabc2897. [CrossRef] [PubMed]
14. Zheng, L.; Zhou, Z.; Sun, P.; Zhang, Z.; Wang, R. A novel control mode of bionic morphing tail based on deep reinforcement learning. *arXiv* **2020**. [CrossRef]
15. Murayama, Y.; Nakata, T.; Liu, H. Aerodynamic performance of a bird-inspired morphing tail. *J. Biomech. Sci. Eng.* **2023**, *18*, 22–00340. [CrossRef]

16. Chang, E.; Lentink, D. Biohybrid morphing tail aerial robot. In Proceedings of the 9th Internatinal Symposium on Adaptive Motion of Animals and Machines, Lausanne, Switzerland, 20–23 August 2019.
17. Parga, J.R.; Reeder, M.F.; Leveron, T.; Blackburn, K. Experimental study of a micro air vehicle with a rotatable tail. *J. Aircr.* **2007**, *44*, 1761–1768. [CrossRef]
18. Gamble, L.L.; Inman, D.J. A tale of two tails: Developing an avian inspired morphing actuator for yaw control and stability. *Bioinspiration Biomim.* **2018**, *13*, 026008. [CrossRef] [PubMed]
19. Pérez Sanchez, V.; Gómez Tamm, A.E.; Savastano, E.; Arrue, B.C. Bio-Inspired Morphing Tail for Flapping-Wings Aerial Robots Using Macro Fiber Composites. *Appl. Sci.* **2021**, *11*, 2930. [CrossRef]
20. Barcala-Montejano, M.A.; Rodríguez-Sevillano, A.; Crespo-Moreno, J.; Bardera Mora, R.; Silva-González, A.J. Optimized performance of a morphing micro air vehicle. In Proceedings of the 2015 International Conference on Unmanned Aircraft Systems (ICUAS), Denver, CO, USA, 9–12 June 2015; IEEE: New York, NY, USA, 2015; pp. 794–800.
21. Bardera, R.; Rodríguez-Sevillano, A.A.; García-Magariño, A.; Barroso, E. Wake Measurements of a MAV with Morphing Geometry. In Proceedings of the 8th European Conference for Aeronautics and Space Sciences (EUCASS), Madrid, Spain, 1–4 July 2019.
22. Barroso Barderas, E.; Bardera Mora, R.; Rodríguez-Sevillano, A.A.; Matías García, J.C. Numerical Analysis of Bioinspired Tails in a Fixed-Micro Air Vehicle. *Aerospace* **2023**, *10*, 793. [CrossRef]
23. Barroso Barderas, E.; Rodríguez-Sevillano, A.A.; Barderas Mora, R.; Crespo Moreno, J.; Matías García, J.C. Design of Non-Conventional Flight Control Systems for Bioinspired Micro Air Vehicles. *Drones* **2022**, *6*, 248. [CrossRef]
24. Barderas, E.B.; Bardera, R.; Rodríguez-Sevillano, Á.; Matias-Garcia, J.C.; Muñoz-Campillejo, J. Experimental Analysis of the T-Tail Vortex effect in a Bioinspired Micro Air Vehicle. In Proceedings of the AIAA Aviation Forum, Chicago, IL, USA, 27 June–1 July 2022.
25. Mueller, T.J. *Introduction to the Design of Fixed-Wing Micro Air Vehicles*; American Institute of Aeronautics and Astronautics: Reston, VA, USA, 1982.
26. Carmichael, B.H. *Low Reynolds Number Airfoil Survey, Volume 1*; Technical Report NASA-Cr-154803-Vol-1; National Aeronautics and Space Administration: Washington, DC, USA, 1981.